



# Efficient removal of bisphenol A and Cr(VI) simultaneously in an advanced redox photoelectrocatalytic system over dual 3D TiO<sub>2</sub> photoelectrodes

Yiqiong Hu<sup>a</sup>, Yuzhou Jin<sup>a</sup>, Pan Zhang<sup>a</sup>, Ya-nan Zhang<sup>a,b,\*</sup>, Guohua Zhao<sup>a,b,\*</sup>

<sup>a</sup> School of Chemical Science and Engineering, Shanghai Key Lab of Chemical Assessment and Sustainability, Tongji University, Shanghai 200092, People's Republic of China

<sup>b</sup> Key Laboratory of Yangtze River Water Environment, Tongji University, Shanghai 200092, People's Republic of China

## ARTICLE INFO

### Keywords:

Bisphenol A  
Cr(VI)  
Simultaneous removal  
Synergistic photoelectrocatalytic system  
3D FH-TiO<sub>2</sub>/Ti

## ABSTRACT

An adventurous strategy on the premise of synergistic photoelectrocatalysis (PEC) system based on three-dimensional (3D) TiO<sub>2</sub> is proposed to realize the simultaneous removal of BPA and Cr(VI). The TiO<sub>2</sub> photoelectrode demonstrates a 3D configuration, meanwhile supplies a multilevel facet heterojunction (FH). The dual-FH-TiO<sub>2</sub>/Ti PEC system is constructed via the application of 3D FH-TiO<sub>2</sub>/Ti as both cathode and anode, where the redox efficiency of BPA and Cr(VI) increased by 1.07 and 4.28 times of the single system. The visible growth accounts for more exposure of active sites and a higher utilization of active species, proved by EPR and quenching experiments. In the practical wastewater, the removal efficiency of BPA and Cr(VI) reaches 97.04% and 81.18% in 1 h. The effects of various influence factors such as pH, electrolyte concentration and coexisting ions on BPA and Cr(VI) removal are studied for practical applications.

## 1. Introduction

With the acceleration of industrialization worldwide, industrial wastewater increasingly become one of the main sources of water pollution for its high toxicity. Heavy metals [1–3] and endocrine disrupting compounds (EDCs) [4–6] are frequently detected, coexisting in the industrial wastewater, which pose a serious threat to human life. Bisphenol A (BPA) is one of representative EDCs, whose total annual production in China reaches nearly 1 million tons, giving rise to serious carcinogenicity [7,8]. Meanwhile, the emission of hexavalent chromium (Cr(VI)), the typical toxic heavy metal, rapidly grows with the development of leather tanning and other industries [9,10]. Currently, the coexistence of BPA and Cr(VI) are often discovered in sewage water, which are urgent to realize the simultaneous removal [11–13].

Traditional technologies including biodegradation and adsorption techniques have made a great of progresses on water treatment, however still trapped in time-consuming property and low removal efficiency [14–16]. Additionally, the above methods have limitations in the simultaneous removal of multiple pollutants in complex water bodies. Advanced oxidation technologies such as photocatalytic (PC) method make the simultaneous elimination of BPA and Cr(VI) come true by driving redox reaction, but the separation of photoexcited carriers is

constrained for the morphology of powder materials, and the further improved removal performance should be given wide and warm concern [17–20]. Photoelectrocatalytic (PEC) process taking full advantage of PC and EC techniques, is able to rapidly implement the charge separation and easily realize the recovery of catalyst [21–24]. The spatial separation of redox reaction is advantageous to the simultaneous elimination of BPA and Cr(VI). Since that PEC is a heterogeneous catalytic reaction, greatly depending on the interface activity, building a high-efficient photoelectrode is an ideal tactic to reach an effective removal.

TiO<sub>2</sub>, one of promising PEC materials, has been widely used in the water treatment field. At present, a series of facet-dependent TiO<sub>2</sub> materials like anatase {001} faceted TiO<sub>2</sub> and rutile {111} faceted TiO<sub>2</sub>, with competent catalytic activity have already been obtained via crystal facet engineering [25–27]. Ulteriorly, it is reported that the separation of photogenerated charges can be effectively prompted, when multiple facets coexist to form facet heterojunction (FH). And the 2D FH such as {001}/{101} and {111}/{110} has been mainly investigated [28–30].

Herein, we propose to construct an advanced photoelectrode with multilevel FHs, manifesting a three-dimensional (3D) configuration. The 3D FH-TiO<sub>2</sub>/Ti is fabricated via an in situ growth of ordered 1D rutile nanorods on Ti mesh substrate and subsequently epitaxial growing

\* Corresponding authors at: School of Chemical Science and Engineering, Shanghai Key Lab of Chemical Assessment and Sustainability, Tongji University, Shanghai 200092, People's Republic of China.

E-mail addresses: [yananzhang@tongji.edu.cn](mailto:yananzhang@tongji.edu.cn) (Y.-n. Zhang), [g.zhao@tongji.edu.cn](mailto:g.zhao@tongji.edu.cn) (G. Zhao).

<https://doi.org/10.1016/j.apcatb.2022.122102>

Received 21 February 2022; Received in revised form 24 September 2022; Accepted 23 October 2022

Available online 26 October 2022

0926-3373/© 2022 Elsevier B.V. All rights reserved.

nanocones based on a secondary hydrothermal method. The 3D multi-level FHs ({110}/{101}/{111}) are acquired according to constructing the co-exposed {110}, {101} and {111} facets. Moreover, a synergetic system is following constructed via the dual utilization of 3D FH-TiO<sub>2</sub>/Ti in the role of cathode and anode, realizing the simultaneous treatment of BPA and Cr(VI). At first, 3D advanced configuration provides high specific surface, propitious to the adsorption of pollutants. Secondly, the matched electronic band structure of {110}, {101} and {111} facets leads to the efficient charge separation. Thirdly, the simultaneous removal of BPA and Cr(VI) is achieved via the efficient PEC oxidation of BPA at the anode and the effective PEC reduction from Cr(VI) to Cr(III) at the cathode. The synergistic effect of redox reaction brings about the deep elimination of these two pollutants. And the 3D FH-TiO<sub>2</sub>/Ti photoelectrode can be cushily tailored for its in situ fabrication on flexible Ti mesh, satisfying the requirement in practical applications. Our work offers a sustainable and economically viable route for simultaneous treating wastewater containing heavy metals and EDCs.

## 2. Experimental

### 2.1. Preparation of 3D FH-TiO<sub>2</sub>/Ti

3D FH-TiO<sub>2</sub>/Ti was facilely prepared via two steps: the in situ synthesis of 1D TiO<sub>2</sub> nanorods, and the following growth of second-level nanocones. Primarily, the Ti mesh (2.5 cm × 3.5 cm) was pretreated in the chemical polish solution (V<sub>H<sub>2</sub>O</sub>: V<sub>HNO<sub>3</sub></sub>: V<sub>HF</sub>=25:5:1) within 30 s. Subsequently, the Ti substrate was placed on a 100 mL Teflon hollow cylindrical support, approximately 7 cm apart from the mixed solvent, containing HCl (1.3 mL), H<sub>2</sub>O<sub>2</sub> (300 μL) and deionized water (5.0 mL). After a 5 h reaction at 200 °C, the precursor was flushed thoroughly with deionized water and dried at room temperature (named 1D TiO<sub>2</sub>/Ti).

3D FH-TiO<sub>2</sub>/Ti was fabricated by a secondary hydrothermal method for the growth of nanocones. Concisely, 210 μL HCl and 125 μL TiCl<sub>3</sub> were dissolved in 25 mL deionized water to form mixed solution. Then, the solution was transferred into a 100 mL Teflon-lined stainless steel autoclave with the 1D TiO<sub>2</sub>/Ti precursor for a 4 h treatment at 80 °C. All of the photoelectrodes were annealed at 450 °C for 120 min in air.

### 2.2. Characterization methods

The morphologies of photoelectrodes were obtained by scanning electron microscopy (SEM, Hitachi-S4800) and transmission electron microscopy (TEM, JEM-2100, JEOL). The crystal phase and structures of materials were detected by X-ray diffraction (XRD, D8 Advance Bruker) over the 2θ range of 20 – 80°. In order to investigate the element composition, X-ray photoelectron spectroscopy (XPS, <10<sup>-8</sup> torrent, Al target, 150 W, AXIS Ultra DLD, Shimazu Kratos) was applied. The light absorption performances of the photoelectrodes were recorded by UV-vis diffuse reflection spectroscopy (DRS, Carry 5000, Agilent Co, America) from 300 to 600 nm. Photoluminescence spectrophotometer (PL, F-7000, Japan) was used to explore the charge separation efficiency with a 410 nm excitation wavelength. The PL lifetime was characterized by a time-resolved fluorescence spectrometer (TRPL, HORIBA Fluorolog-3-11).

Additionally, the PEC performance was measured via the CHI 660c electrochemical workstation employed in a three-electrode system, where the 3D FH-TiO<sub>2</sub>/Ti, saturated calomel electrode (SCE) and platinum plate offered the function as working electrode, reference electrode and counter electrode, respectively. The UV-Vis light source was 500 W LA-410UV-3 lamp (Solar 500, Nbet Technology Co. Ltd., Beijing, China), fixed with 1 cm distance from the working electrode during the PEC process.

### 2.3. Experimental set-up and procedure of photoelectrocatalytic redox

The PEC removal experiment was performed in a 50 mL quartz

reactor irradiated by a 300 W xenon lamp under the wavelength of 320–780 nm (PLS-SXE300, Perfect Light Technology Co. Ltd., Beijing, China). The initial concentration of Cr(VI) and BPA were 5 mg/L. The 0.1 M Na<sub>2</sub>SO<sub>4</sub> played a role in supporting electrolyte. The BPA oxidation were carried out at + 0.4 V vs. SCE in 60 min, while the Cr(VI) reduction was at – 0.4 V vs SCE. Otherwise the simultaneous removal of these two pollutants was also conducted at + 0.4 V. The concentrations of BPA during the oxidation period were tested by the HPLC (Agilent 1260). The corresponding mobile phase was 35:65 (v/v) water/ methanol mixture with the flow rate of 0.8 mL/min. The UV detector wavelength was 225 nm. The concentrations of Cr(VI) were determined through the 1,5-Diphenyl carbazide method, analyzed by the UV-vis spectrophotometer (Shimadzu UV1800, Japan).

### 2.4. Detailed scavenging experiment and intermediate detection of BPA

The scavenging experiment was conducted based on the above procedures with the addition of isopropyl alcohol (IPA), plenty nitrogen (N<sub>2</sub>), disodium EDTA (EDTA-2Na), L-histidine and CCl<sub>4</sub> as the quenchers for •OH, O<sub>2</sub><sup>•-</sup>, h<sup>+</sup>, <sup>1</sup>O<sub>2</sub>, e<sup>-</sup>, respectively. With the increase of the dosage of the above quenching agents, the BPA oxidation and Cr(VI) reduction reached saturation ultimately.

Gas chromatography-mass spectrometry (GC-MS) was performed to obtain the intermediates of BPA oxidation. The degradation solution underwent extraction with CH<sub>2</sub>Cl<sub>2</sub> 3 times. The volume ratio of the degradation solution and CH<sub>2</sub>Cl<sub>2</sub> was 1:1. The obtained organic phase was dehydrated with anhydrous sodium sulfate, then filtered and concentrated to 2 mL.

### 2.5. Density function theory (DFT) calculations

The electronic structures of three facets ({110}, {101} and {111}) were calculated by first principle calculation based on DFT. The projector augmented wave (PAW) approach implemented in the Vienna ab initio package (VASP) was applied to treat the valance electrons described by cut-off plane waves and core electrons described by pseudo wave functions. The energy cut-off was set as 600 eV for static ground state energy and electronic structure. The Perdew-Burke-Ernzerhof (PBE) functional on the basis of generalized gradient approximation (GGA) was used to calculate the exchange-correlation interaction. Γ-centered k-mesh in the Brillouin zone was applied for the k-space integration in electronic energy calculation in all steps of 6 × 7 × 1 for {101}, 8 × 4 × 1 for {110} and 6 × 6 × 1 for {111}. In all calculation, the Hubbard U value of U(Ti-3d) = 4.2 eV was employed to ensure appropriate electronic structure. The cut-off energy of 400 eV was used to optimize the slab models with convergence limit of electronic energy of 1 × 10<sup>-6</sup> eV and force of 0.02 eV/Å. Cell optimization was calculated with cut-off energy of 600 eV and self-consistent force less than 0.01 eV/Å for rutile before construction of the slab models. The tetrahedron integral was used to calculate the density of states (DOS).

## 3. Results and discussion

### 3.1. 3D FH-TiO<sub>2</sub>/Ti photoelectrode characterization

The morphologies of photoelectrodes were distinctly presented in Fig. 1 and Fig. S1. At first, a 3D network structure of substrate Ti mesh was observed in Fig. S1a, greatly improving the specific surface area. Additionally, the prepared TiO<sub>2</sub> directly and uniformly grew on the Ti mesh, engendering a rough surface, in which sufficient active sites were exposed (Fig. S1b). The SEM image of Fig. 1a-c indicated that 1D vertical nanorods were in situ grown on the Ti mesh substrate (1D TiO<sub>2</sub>/Ti) via a facile hydrothermal treatment. Its top surface performed a pyramidal-shaped uplift with approximately 300 nm in diameter, which was further confirmed as the {111} facet by HRTEM result (Fig. 1g), since that the two perpendicular lattice fringes were measured as 0.323 nm



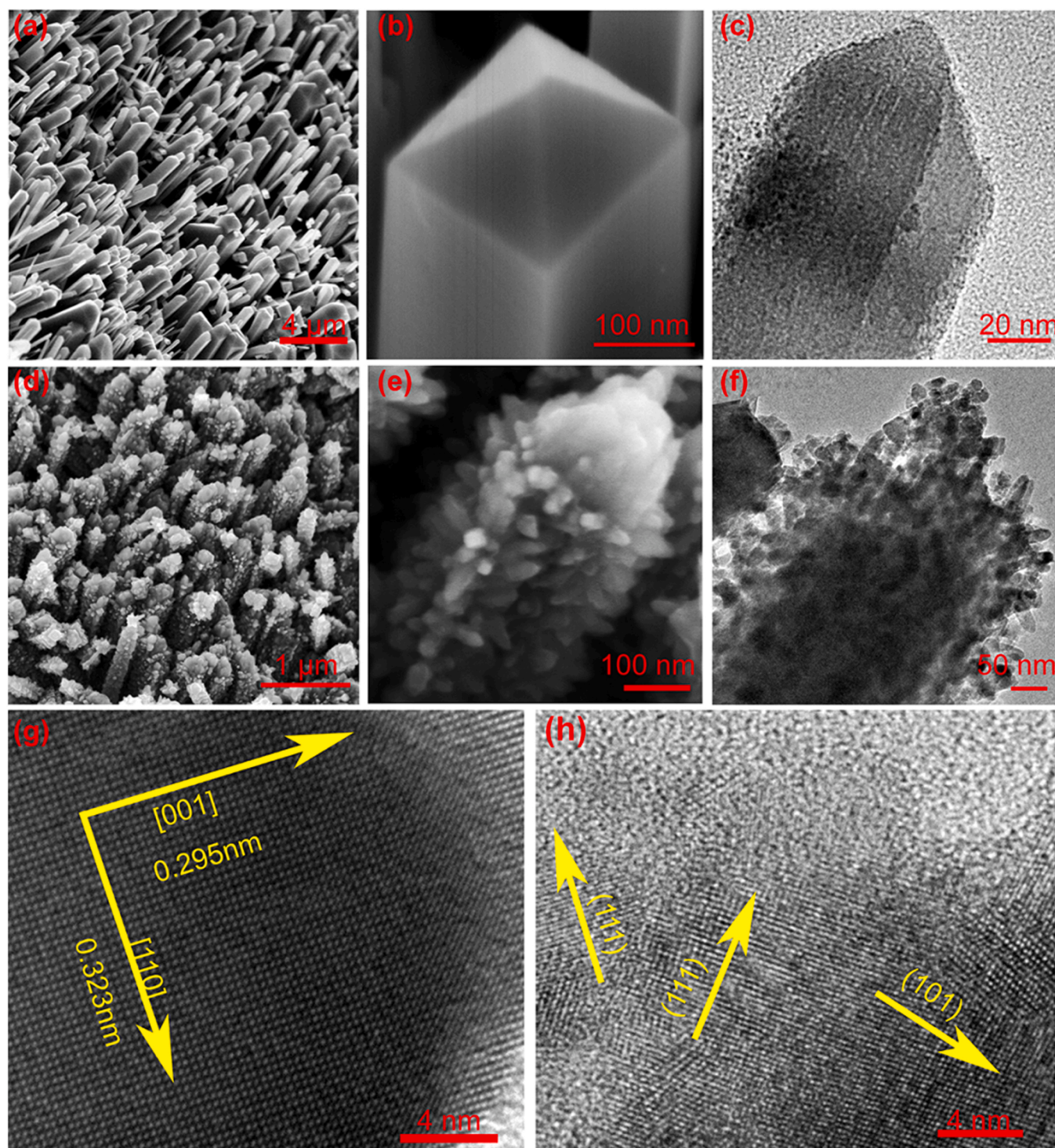


Fig. 1. SEM and TEM images of 1D  $\text{TiO}_2/\text{Ti}$  (a-c) and 3D FH- $\text{TiO}_2/\text{Ti}$  (d-f); HRTEM images of 3D FH- $\text{TiO}_2/\text{Ti}$  (g-h).

and 0.295 nm tallied with (110) and (001) planes [30]. After a secondary hydrothermal fabrication (Fig. 1d-f), the obtained target photoelectrode displayed a 3D configuration with the growth of nanocones as secondary structures (3D FH- $\text{TiO}_2/\text{Ti}$ ). The numerous nanocones with diameter of 35 nm and 66 nm in length densely attached to the well-aligned nanorods. In comparison with the nanorod structure, the nanocones structure was proved to be conducive to the rapid diffusion of water, thus were beneficial for the mass transport in the removal process [31]. The HRTEM image in Fig. 1h indicated that the fringe spacing of 0.25 and 0.22 nm corresponded to the orientation of d[101]

and d[111] vest in nanocones, implying the coexistence of {101} and {111} facets on nanocones [32]. These results verified that the fabricated 3D FH- $\text{TiO}_2/\text{Ti}$  photoelectrode exhibited a 3D configuration equipped with {110}, {101} and {111} facets.

The light absorption capacity of the obtained photoelectrodes was investigated via DRS. As depicted in Fig. S2, a broader light absorption threshold at about 407 nm was observed over 3D FH- $\text{TiO}_2/\text{Ti}$ , in comparison with that of 1D  $\text{TiO}_2/\text{Ti}$  (403 nm), indicating that the epitaxially grown secondary nanocones were beneficial to light absorption. Since that only the very tiny  $\text{TiO}_2$  nanoparticles (<10 nm) presented the blue

shift of the absorption wavelength originated from the quantum size effect [33], the obtained 1D TiO<sub>2</sub>/Ti and 3D FH-TiO<sub>2</sub>/Ti photoelectrodes both exhibited stable light absorption. Furthermore, the crystalline phases of photoelectrodes were characterized by XRD (Fig. S3). Fig. S3a exhibited the typical diffraction peaks of 1D TiO<sub>2</sub>/Ti corresponding to rutile phase, which suitably matched the (110), (101), (111), (211), (002), (301) and (112) planes of rutile TiO<sub>2</sub> (JCPDS No. 21-1276) [32]. Additionally, the 3D FH-TiO<sub>2</sub>/Ti photoelectrode composed of nanorods and nanocubes was proved with the same rutile phase, demonstrating tetragonal crystal structures. And the rest with a star mark were belonged to Ti mesh substrate (JCPDS No. 01-089-5009) [34]. Then the XPS patterns were examined to analysis the surface chemical bonding states of as-prepared photoelectrodes. Apparently, both 1D TiO<sub>2</sub>/Ti and 3D FH-TiO<sub>2</sub>/Ti photoelectrodes were made up of Ti and O elements in Fig. S3b. The Ti 2p<sub>3/2</sub> and Ti 2p<sub>1/2</sub> of Ti<sup>4+</sup> peaks (Fig. S3c) seated at 457.8 and 463.4 eV were clearly observed on 3D FH-TiO<sub>2</sub>/Ti. As shown in Fig. S3d, the O 1s spectrum were examined at 529.6 and 531.9 eV, corresponding to Ti-O and Ti-O-H [35,36]. As seen above, in contrast to 1D TiO<sub>2</sub>/Ti, approximately 0.5 eV shifted toward higher binding energies of Ti spectrum could be observed on 3D FH-TiO<sub>2</sub>/Ti, which indicated that Ti atom was electron donor, leading to a decrease in the electron density [37]. And the enhancement about the area ratio of peak Ti-O-H to peak Ti-O was observed with the growth of secondary nanocubes, demonstrating more surface defects caused by oxygen vacancy [38]. As Ti<sup>3+</sup> and oxygen vacancies were simultaneously formed [39], it could also be speculated the presence of Ti<sup>3+</sup> from 3D FH-TiO<sub>2</sub> lattice, paving to the enhanced light absorption, which was consistent with the DRS results.

### 3.2. Highly efficient redox performance of 3D FH-TiO<sub>2</sub>/Ti photoelectrode

The 3D FH-TiO<sub>2</sub>/Ti was firstly used as the anode to investigate the removal efficiency of BPA, while the Pt plate acted as the cathode. The results in Fig. 2a illustrated that almost 100% of BPA could be oxidized in 60 min on 3D FH-TiO<sub>2</sub>/Ti, significantly higher than that of 1D TiO<sub>2</sub>/Ti (88.41%). Fig. 2b displayed that the first order kinetic constant (*k*) of 3D FH-TiO<sub>2</sub>/Ti was 0.084 min<sup>-1</sup>, 2.1 fold that of 1D TiO<sub>2</sub>/Ti. Next, as manifested in Fig. 2c, 63.46% of Cr(VI) was reduced on 3D FH-TiO<sub>2</sub>/Ti in its role of cathode when the Pt plate was as the anode, while 1D TiO<sub>2</sub>/Ti realized only 55.32% reduction of Cr(VI). A higher second-order *k* value was gained on 3D FH-TiO<sub>2</sub>/Ti (0.032 M<sup>-1</sup> min<sup>-1</sup>) than that on 1D TiO<sub>2</sub>/Ti (0.019 M<sup>-1</sup> min<sup>-1</sup>), illustrating a faster reduction rate (Fig. 2d). Obviously, 3D FH-TiO<sub>2</sub>/Ti exhibited more potent elimination ability on both BPA and Cr(VI) removal.

The more prominent removal performance of 3D FH-TiO<sub>2</sub>/Ti above was as a result of its 3D configuration and the spatial separation of photo-excited e<sup>-</sup>/h<sup>+</sup>. An elevated specific surface area was achieved through the construction of a 3D configuration, which worked to the adsorption processes. The static adsorption properties of photoelectrodes were following recorded in Fig. 3a-b. Within 1 h, the saturated adsorption of BPA on 3D FH-TiO<sub>2</sub>/Ti and 1D TiO<sub>2</sub>/Ti were up to 63.28 and 12.03 mg/g, respectively. As for Cr(VI), after 40 min, the adsorption capacity of 3D FH-TiO<sub>2</sub>/Ti reached 45.37 mg/g, which was nearly 1.71 times that of 1D TiO<sub>2</sub>/Ti. Obviously, the 3D FH-TiO<sub>2</sub>/Ti showed the slight increased adsorption capacity. The results indicated more adsorption sites exposed in the 3D configuration, which was further employed via in situ ATR-FTIR spectroscopy. Displayed in Fig. 3c, upward infrared vibrations appeared at wave number of 1463 cm<sup>-1</sup> and 1223 cm<sup>-1</sup>, which were ascribe to the bending vibration

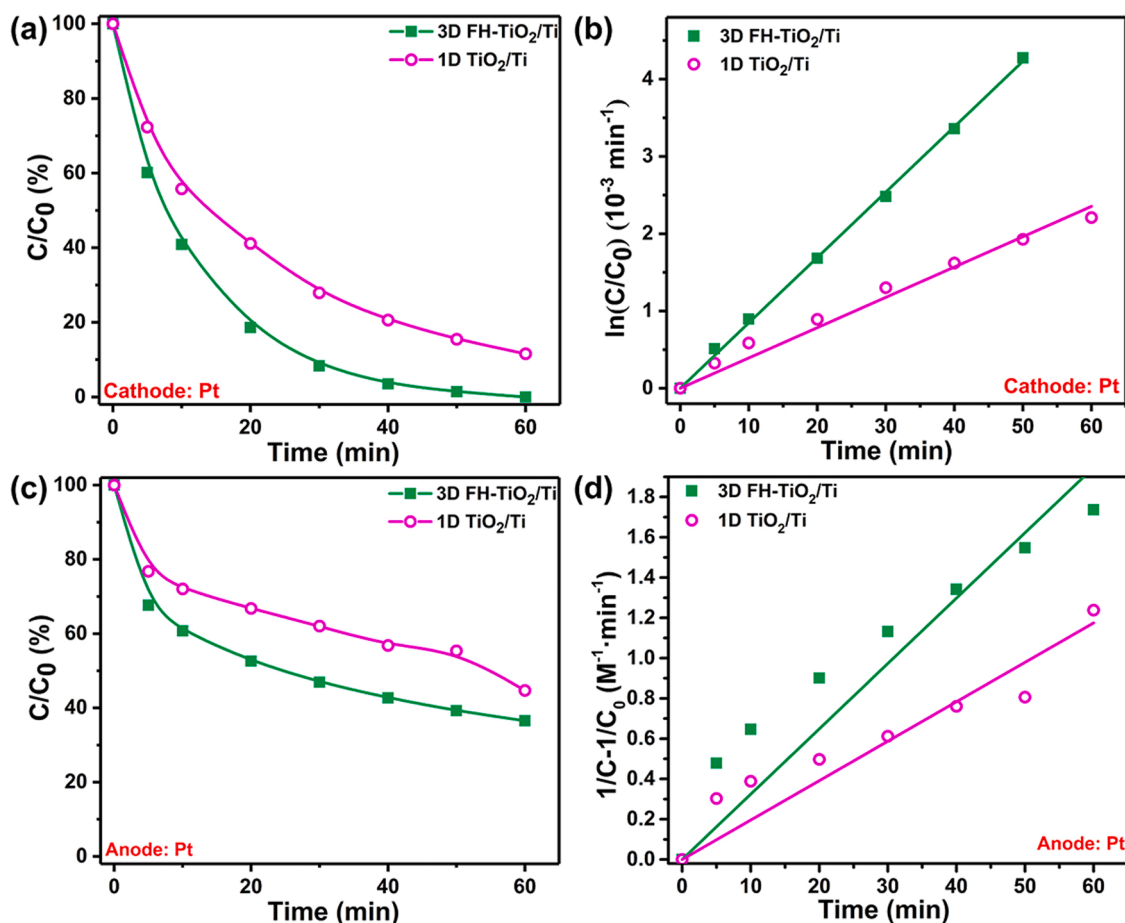
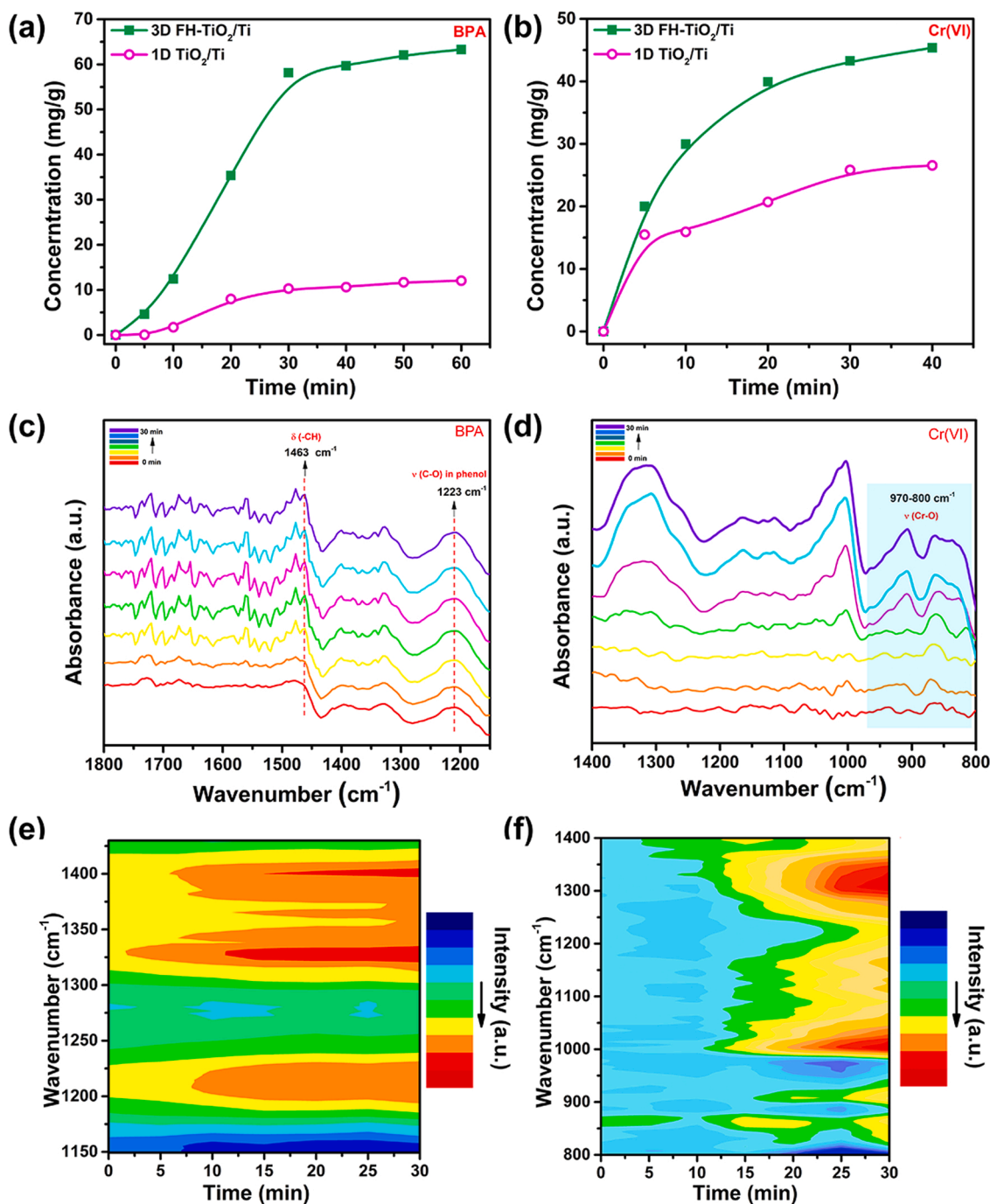


Fig. 2. The removal plots and rate constant curves for BPA oxidation (a-b) and Cr(VI) reduction (c-d) on 1D TiO<sub>2</sub>/Ti and 3D FH-TiO<sub>2</sub>/Ti.





**Fig. 3.** The static adsorption of BPA (a) and Cr(VI) (b) over 1D TiO<sub>2</sub>/Ti and 3D FH-TiO<sub>2</sub>/Ti; in situ ATR-FTIR spectra of BPA (c) and Cr(VI) (d) on 3D FH-TiO<sub>2</sub>/Ti; the contour plots of in situ ATR-FTIR peak intensity of BPA (e) and Cr(VI) (f).

of alkyl group and C-O in phenol. Moreover, the position of C-O peak showed a red shift relative to standard BPA, indicating that BPA was chemically adsorbed on 3D FH-TiO<sub>2</sub>/Ti [40–43]. In Fig. 3d, the spectral range from 970 to 800 cm<sup>-1</sup> mainly exhibited positive absorbance features, owing to the Cr–O stretching vibrations of adsorbed Cr(VI). For more intuitive observation, the contour plots of in situ ATR-FTIR peak intensity were presented in Fig. 3e–f. And the results indicated that the peaks above showed an enhanced trend over time, meaning an increase adsorption of BPA and Cr(VI) [44,45].

The PEC performances of two photoelectrodes were subsequently tested. As demonstrated in Fig. S4a, the amperometric I–t curve of 1D TiO<sub>2</sub>/Ti was 0.24 mA cm<sup>-2</sup>. While with the development of nanocones, the higher anodic photocurrent (0.32 mA cm<sup>-2</sup>) was generated for the

3D FH-TiO<sub>2</sub>/Ti photoelectrode under illumination. A relatively higher donor density ( $N_D$ ,  $5.54 \times 10^{20}$  cm<sup>-3</sup>) of 3D FH-TiO<sub>2</sub>/Ti in Fig. S4b implied the enhanced separation of photogenerated carriers, in contrast to that of  $3.21 \times 10^{20}$  cm<sup>-3</sup> of 1D TiO<sub>2</sub>/Ti. And in a distinct comparison with 1D TiO<sub>2</sub>/Ti (1320  $\Omega$ ), 3D FH-TiO<sub>2</sub>/Ti exhibited the obviously decreased charge transfer impedance (620  $\Omega$ ) in Fig. S4c, suggesting the elevated charge transfer kinetics. The excellent PEC activity was thought to result from better charge separation and transfer efficiency, therefore, PL and TRPL spectroscopy were employed to further analyze the separation efficiency and the lifetime of the charge carriers. Fig. 4a elucidated that the PL peak intensity of 3D FH-TiO<sub>2</sub>/Ti at 410 nm was much lower than that of 1D TiO<sub>2</sub>/Ti, implying a limited recombination of carriers. The TRPL results (Fig. 4b) showed the distinctly enhanced

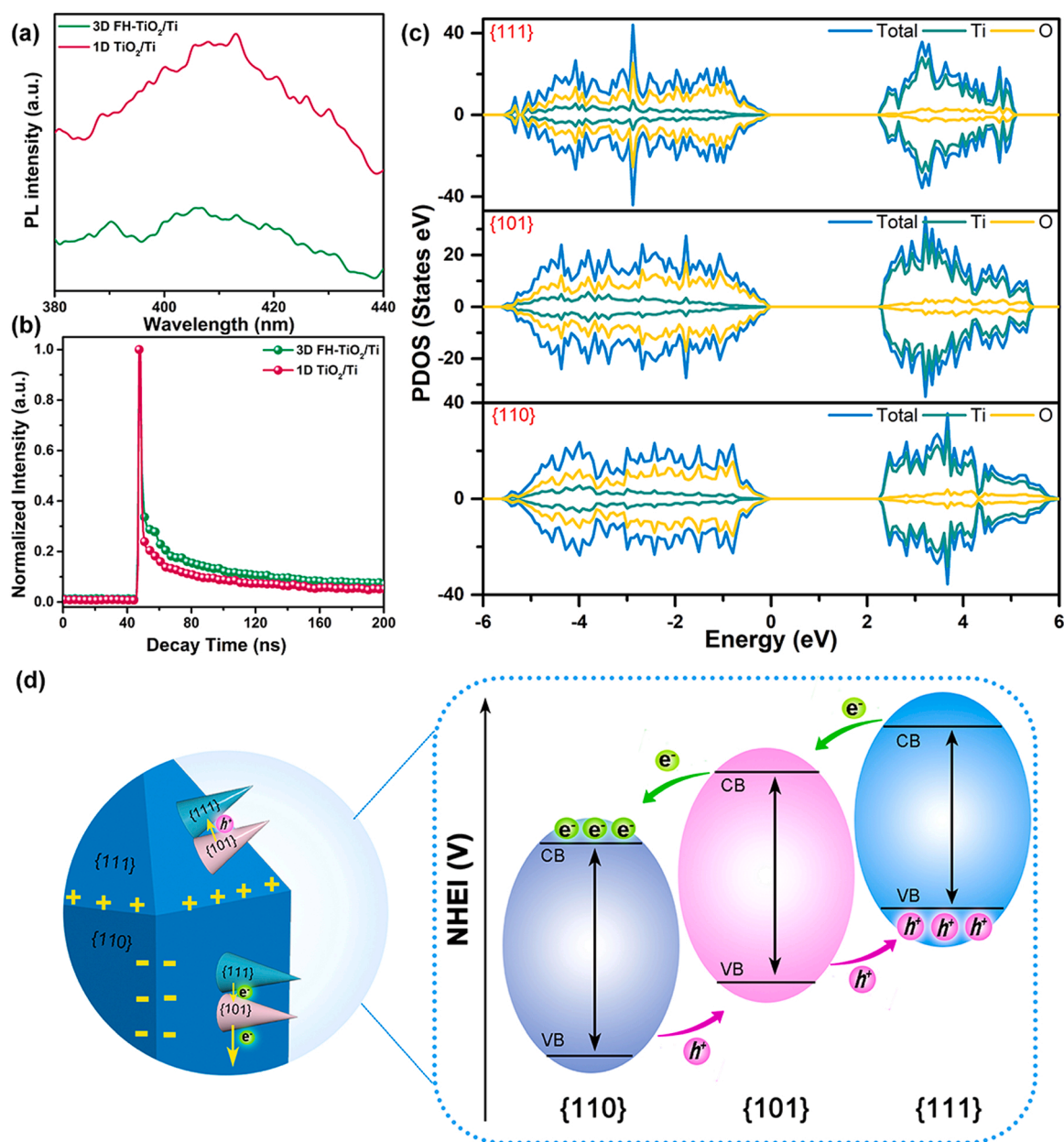


**Fig. 4.** PL spectra (a) and transient fluorescence (b) of 1D TiO<sub>2</sub>/Ti and 3D FH-TiO<sub>2</sub>/Ti; (c) Calculated PDOS on Ti and O elements of 3D FH-TiO<sub>2</sub>/Ti with {111}, {101} and {110} facets (d) Schematic diagram of charge transfer between {111}, {101} and {110} facets over 3D FH-TiO<sub>2</sub>/Ti photoelectrode.

average emission lifetime of 3D FH-TiO<sub>2</sub>/Ti (10.25 ns), compared with 1D TiO<sub>2</sub>/Ti (10.02 ns), which was ascribed to promoted charge separation.

Thus, combined with the density functional theory (DFT) calculations [26,46], the separation and migration mechanism of photo-generated e<sup>-</sup>/h<sup>+</sup> was researched in depth. As presented in Fig. S5, the band structures of {110}, {101} and {111} facets with stepped distribution characteristics, were conducive to charge separation and transfer. The partial density of states (PDOS) results were shown in Fig. 4c. The PDOS results presented that all conduction bands (CB) and valence bands (VB) of {110}, {101} and {111} were composed of Ti and O elements, respectively. Among the three facets above, the most enhanced PDOS of {111} facet was observed near the VBM, which exhibited stronger electronic activity, paving the photogenerated electrons on {111} facet transfer from VBM to CBM [47]. Besides, the PDOS on the CB of {110} facet distributed more widely, indicating the photoinduced electrons were itinerant in a broader CB [48]. And the

highest electron density of bottom CB were obtained on {110} facet, indicating the final accumulation of electrons. Thus, a schematic diagram was given in Fig. 4d, realizing the final aggregation of photo-generated h<sup>+</sup> as well as e<sup>-</sup> on high-reactive {111} and {110} facets, respectively, which was consistent with the results in our previous research [49]. Moreover, the accumulative e<sup>-</sup> smoothly migrated along the nanorods to the substrate, finally reached the cathode. With the joint efforts of 3D configuration and FHs structure, a more complete separation of photo-induced carriers was realized.

Then, the exploration on the degradation mechanism was preliminary implemented. The possible main active species (h<sup>+</sup>, <sup>1</sup>O<sub>2</sub>, ·OH and O<sub>2</sub><sup>-</sup>) in the BPA oxidation process were probed in Fig. S6a with the addition of EDTA-2Na, L-histidine, IPA and the sufficient N<sub>2</sub> in turn [50,51]. The removal efficiency of BPA on 3D FH-TiO<sub>2</sub>/Ti photoanode was declined sharply from 99.39% to 33.86% with the capture of h<sup>+</sup>, indicating the critical role of h<sup>+</sup> in PEC oxidation of BPA in view of a direct transfer process. And progressively inhibition on the BPA removal

efficiency (28.22%, 15.97% and 5.72%) confirmed the effective participation of  $^1\text{O}_2$  and  $\cdot\text{OH}$  in the BPA oxidation, compared with the weak contribution of  $\text{O}_2^{\cdot-}$ . In view of that the cathodic reduction of Cr(VI) mainly depended on the positive effect of electrons,  $\text{CCl}_4$  captured the electrons directly in Fig. S6b, that the removal efficiency decreased from 63.46% to 44.94%, indicating the beneficial devotion of  $e^-$  in Cr(VI) reduction [52]. Besides, the other electrons applied in Cr(VI) reduction on the cathode could be originated from the release of  $\text{O}_2^{\cdot-}$  (Eq. 1) [53]. When  $\text{O}_2^{\cdot-}$  was fully captured, the reduction efficiency of Cr(VI) decreased from 63.46% to 47.23%, confirming a part of contribution on Cr(VI) reduction. Thus, it could be concluded that electrons were beneficial to the reduction of Cr(VI).



### 3.3. Efficiently synchronous removal BPA and Cr(VI) over dual-FH-TiO<sub>2</sub>/Ti PEC system

Based on the results above, the 3D FH-TiO<sub>2</sub>/Ti exhibited excellent oxidation and reduction capacity applied as the anode and cathode, respectively, owing to the optimized 3D configuration and high separation efficiency of photogenerated  $e^-/h^+$ . Therefore, an anodic-cathodic photoelectrochemical (dual-FH-TiO<sub>2</sub>/Ti PEC) system was proposed by the simultaneous utilization of 3D FH-TiO<sub>2</sub>/Ti. Fig. 5a-b pointed out that the oxidation efficiency of BPA in the dual-FH-TiO<sub>2</sub>/Ti PEC system

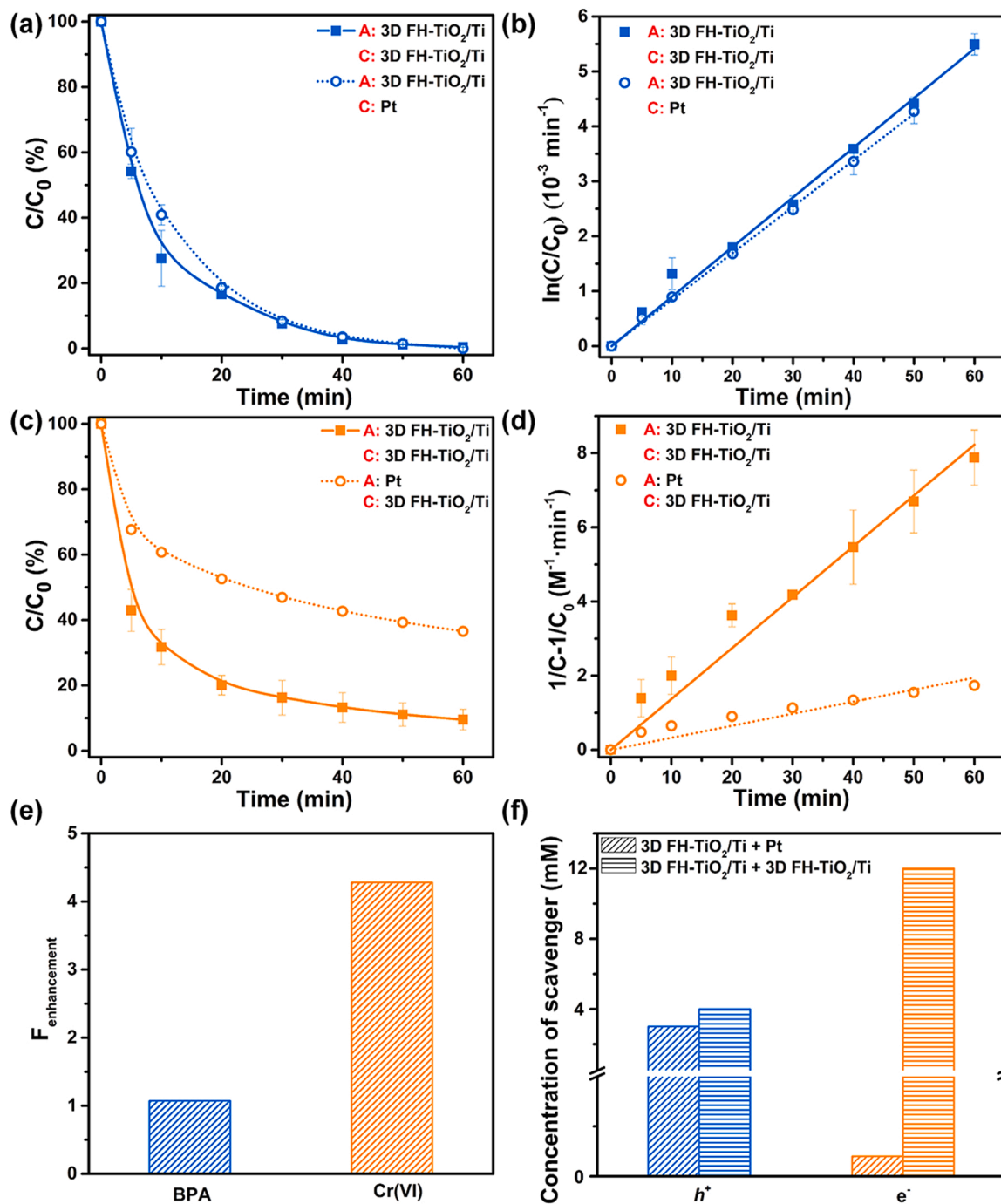


Fig. 5. The BPA oxidation (a) and Cr(VI) reduction (c) efficiency with their corresponding rate constant curves (b and d) in the dual and single FH-TiO<sub>2</sub>/Ti PEC system; (e) The  $F_{\text{enhancement}}$  of BPA and Cr(VI); (f) The saturation concentration of quencher towards  $h^+$  and  $e^-$  in the single and dual-FH-TiO<sub>2</sub>/Ti PEC system.



manifested a visible growth from 81.40% to 83.42% in 20 min, whose  $k$  was also improved from  $0.084 \text{ min}^{-1}$  to  $0.090 \text{ min}^{-1}$ , in contrast to the system with Pt plate as counter electrode (single-FH-TiO<sub>2</sub>/Ti PEC). Furthermore, as shown in Fig. 5c-d, a pleasant surprise was obtained that almost 90.5% of Cr(VI) was reduced in the dual-FH-TiO<sub>2</sub>/Ti PEC system, distinctly compared with that of 63.46% in the single-FH-TiO<sub>2</sub>/Ti PEC system, where the second-order  $k$  increased from 0.032 to  $0.137 \text{ M}^{-1} \text{ min}^{-1}$ , likewise. To quantitatively evaluate the enhanced redox ability in the dual-FH-TiO<sub>2</sub>/Ti PEC system, removal enhancement factor ( $F_{\text{enhancement}}$ , Eq. 2) was calculated below:

$$F_{\text{enhancement}} = \frac{k_{\text{dual}}}{k_{\text{single}}} \quad (2)$$

Where  $k_{\text{dual}}$  and  $k_{\text{single}}$  were the rate constants towards the same pollutant in the dual and single FH-TiO<sub>2</sub>/Ti PEC system, respectively. As illustrated in Fig. 5e, the dual-FH-TiO<sub>2</sub>/Ti PEC system exhibited the 1.07 and 4.28 of  $F_{\text{enhancement}}$  towards BPA and Cr(VI), indicating a greatly promoted removal efficiency.

It could be concluded that the dual-FH-TiO<sub>2</sub>/Ti PEC system presented the consistently pleasant improvement towards the BPA and Cr(VI) removal on the synergistic effect of the cathode and anode. Among them, the rapid development of Cr(VI) reduction profited from that the sufficient photo-excited electrons separated from photoanode were effectively transferred to cathode under applied bias, then were

thoroughly utilized in the cathodic reduction. The active species in synergistic system were researched via EPR technique, since that the removal performance of BPA and Cr(VI) mainly depended on the active species which were obtained within the participation of  $h^+$  and  $e^-$  arising from Eqs. (3–6). The EPR signal peaks (Fig. S7a-c) of DMPO- $\bullet\text{OH}$ , TEMPO- $^1\text{O}_2$  and DMPO- $\text{O}_2^{\bullet-}$  in the dual-FH-TiO<sub>2</sub>/Ti PEC system were significantly higher than those in the single-FH-TiO<sub>2</sub>/Ti PEC system, which proved that more active species were produced in the dual-FH-TiO<sub>2</sub>/Ti PEC system. Fig. S7d manifested the EPR signal intensity ratio of dual-FH-TiO<sub>2</sub>/Ti PEC system to single-FH-TiO<sub>2</sub>/Ti PEC system, which were 1.96 times ( $\bullet\text{OH}$ ), 1.19 times ( $^1\text{O}_2$ ) and 2.05 times ( $\text{O}_2^{\bullet-}$ ), respectively. The results above intuitively reflected higher concentration of active species with the synergistic effect of cathode and anode. The obvious increase of  $\text{O}_2^{\bullet-}$  concentration also explained the obvious improvement of Cr(VI) removal rate in the synergetic system. Since that  $h^+$  and  $e^-$  were the main active species in BPA oxidation and Cr(VI) reduction, respectively, the quenching experiment of  $h^+$  and  $e^-$  in dual-FH-TiO<sub>2</sub>/Ti PEC system was further explored. As depicted in Fig. 5f, the concentration of EDTA-2Na and CCl<sub>4</sub> required to achieve saturation quenching were distinctively enhanced in the dual-FH-TiO<sub>2</sub>/Ti PEC system, which were 1.3 and 600 fold of the single-FH-TiO<sub>2</sub>/Ti PEC system, respectively. It could be seen that more active radicals and electrons were produced and acted on the dual-FH-TiO<sub>2</sub>/Ti PEC system.

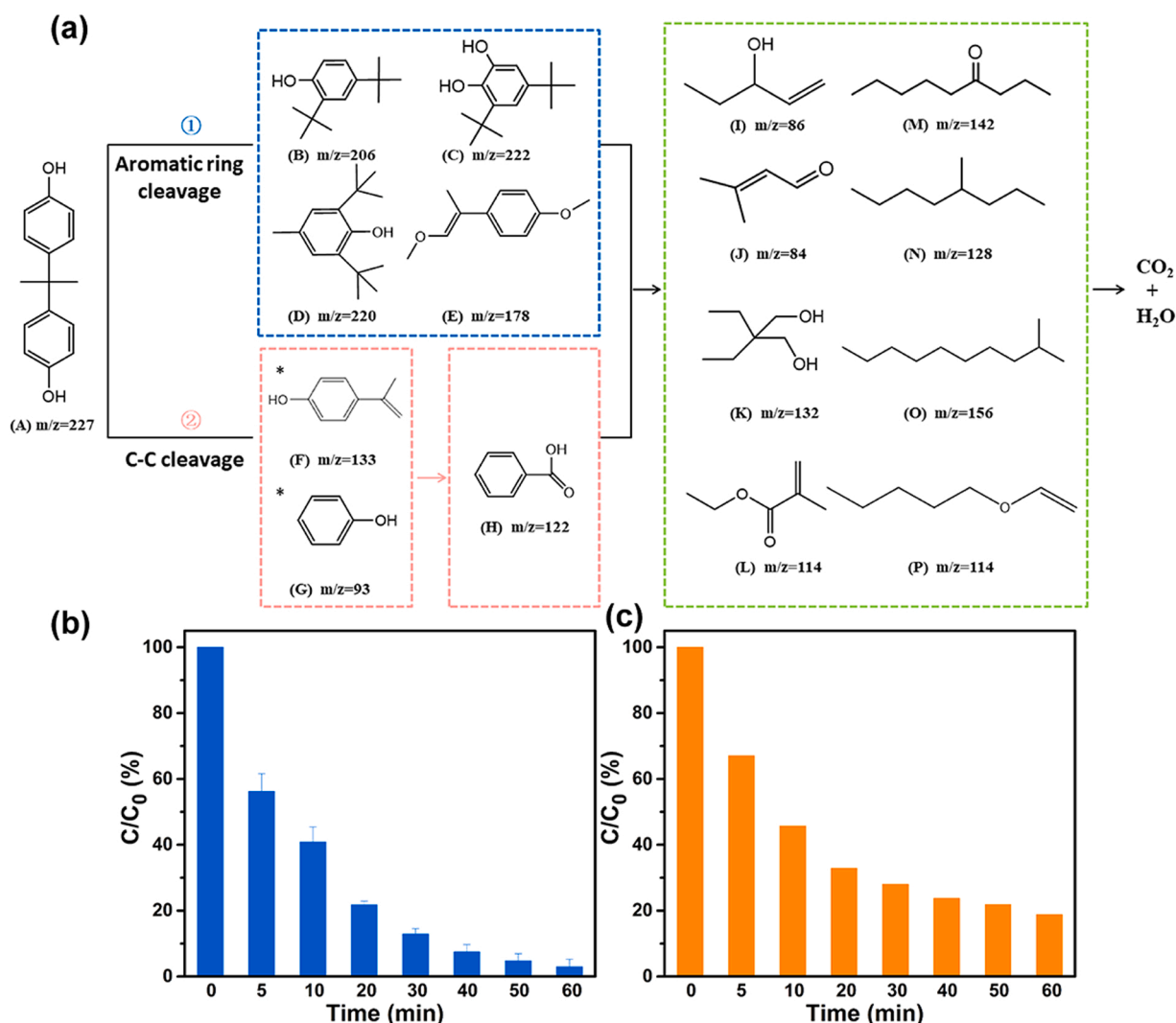


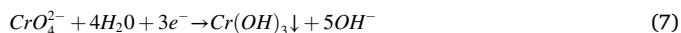
Fig. 6. (a) The PEC degradation pathways of BPA by 3D FH-TiO<sub>2</sub>/Ti photoelectrode; and The removal rate of BPA (b) and Cr(VI) (c) in the practical wastewater.



Besides, the intermediate products of BPA in the dual-FH-TiO<sub>2</sub>/Ti PEC system were detected by GC-MS, and the potential oxidation pathway as well as the whole obtained intermediates were shown in Fig. 6a and Table. S1. Initially, the four intermediates (B-E) in pathway I were produced through the preferential attack of  $\cdot OH$  and  $h^+$ , resulting in the ring cleavage of BPA (A). In pathway II, nucleophilic attack occurred by the reactive species, leading to the C-C bonds scission of benzene rings. As a result, 4-isopropenylphenol (F), phenol (G) and benzoic acid (H) were produced. Finally, low molecular ring-opening products (I-P) were generated through the further oxidation and ring-open reactions. Notably, 2 kinds of ketone compounds were newly discovered, which had not been reported in previous work [54,55]. The chain intermediates ultimately mineralized into CO<sub>2</sub> and H<sub>2</sub>O. Finally, the dual-FH-TiO<sub>2</sub>/Ti PEC system was applied to explore the PEC elimination performance of BPA and Cr(VI) in practical wastewater (Fig. 6b and c). It was surprising that the removal efficiency of BPA and Cr(VI) could reach 97.04% and 81.18% after a 1 h reaction, respectively, forcefully confirming a broad practical application prospect of the dual-FH-TiO<sub>2</sub>/Ti PEC system.

### 3.4. Effects on the PEC elimination of BPA and Cr(VI)

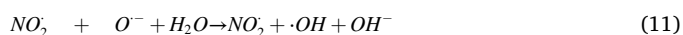
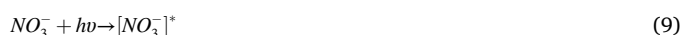
Pollutant elimination depended on many factors, and firstly the impact of pH was delved. As displayed in Fig. S8a-b, the oxidation efficiency towards BPA under acidic or neutral conditions was significantly higher than that under alkaline conditions, among which effective removal (99.38% and 99.69%) was achieved at pH equalled to 5 and 7, respectively. The pH value at 6.8 of zero point charge for TiO<sub>2</sub> inhibited the adsorption of BPA on the charged TiO<sub>2</sub> in its nonionic form, leading to the favorable degradation of BPA in neutral and weak acid aqueous environment. With regard to Cr(VI), the pH influenced the existing states of Cr(VI) ions clearly, where Cr<sub>2</sub>O<sub>7</sub><sup>2-</sup> and HCrO<sub>4</sub><sup>-</sup> predominated at the pH range 2.0–6.0, while only CrO<sub>4</sub><sup>2-</sup> was in a stable existence in solution pH above 6.8 [56]. Fig. S8c showed that the reduction efficiency of Cr(VI) manifested a downward trend as the pH grew, and the related removal rate at pH 9 (0.021 M<sup>-1</sup> min<sup>-1</sup>) fell far behind that in the acid and neutral solution (Fig. S8d). The distinct inhibition was since that followed the reduction of Cr(VI) to Cr(III), abundant of OH<sup>-</sup> at higher pH conditions would prohibit the proceeding of reaction in Eq. 7. Coupled with that the Cr(OH)<sub>3</sub> tended to cover the active sites of the photoelectrode, the Cr(VI) reduction efficiency abated. Different from the results reported in previous literatures that the effective removal of Cr(VI) only obtained in strong acid solution (pH < 4) [9,11], commendable removal performance of 90.46% could be maintained at pH 7 in the dual-FH-TiO<sub>2</sub>/Ti PEC system, demonstrating an excellent reduction ability of this system in a wide pH range.



Secondly, the concentration of Na<sub>2</sub>SO<sub>4</sub> electrolyte was also researched. The oxidation and reduction performance of BPA and Cr(VI) in Fig. S9 both enhanced with the growing concentration from 0.05 M to 0.1 M of Na<sub>2</sub>SO<sub>4</sub>, and the corresponding rates reached 0.039 min<sup>-1</sup> and 0.091 M<sup>-1</sup> min<sup>-1</sup>, respectively. The raised electrolyte concentration positively effected on the solution conductivity and the migration rate of electrons [57]. Nevertheless, a restrained removal performance was observed in 0.2 M Na<sub>2</sub>SO<sub>4</sub> electrolyte, suggesting the occupation of the active sites on photoelectrode via excess electrolyte.

Besides, various ions were detected in sewage water to coexist with BPA and Cr(VI), like the cations Zn<sup>2+</sup>, Mg<sup>2+</sup>, and the anions Cl<sup>-</sup>, NO<sub>3</sub><sup>-</sup> and H<sub>2</sub>PO<sub>4</sub><sup>-</sup>, which might snatch adsorption sites, even the competition

reaction happened on the photoelectrode surface. Therefore, the effects of coexisted cations and anions on respective cathodic and anodic reactions were deeply investigated. In the Fig. S10a-b, the BPA removal rates decreased from 99.46% to 99.16%, 97.85%, and 91.32% in the addition of Cl<sup>-</sup>, H<sub>2</sub>PO<sub>4</sub><sup>-</sup> and NO<sub>3</sub><sup>-</sup> respectively. The first-order  $k$  accordingly declined in contrast to that obtained without adding anions, as well. It indicated the presence of NO<sub>3</sub><sup>-</sup> negatively affected the PEC oxidation of BPA, while Cl<sup>-</sup> and H<sub>2</sub>PO<sub>4</sub><sup>-</sup> affected little. The relatively potent retardation of NO<sub>3</sub><sup>-</sup> on BPA removal, which ascribed to its tendency to adsorb photons, following transformed to NO<sub>2</sub>, the scavenger of  $\cdot OH$  (Eq. 8) [58]. However, NO<sub>3</sub><sup>-</sup> could also result in the formation of  $\bullet OH$  during irradiation with  $\lambda > 280$  nm (Eqs. 9–11), the inhibition on BPA removal with the coexistence of NO<sub>3</sub><sup>-</sup> was lighter than that when  $\cdot OH$  was captured [59].



In regard to the impact of anions, the results were manifested in Fig. S10c-d. The delayed role of Zn<sup>2+</sup> and Mg<sup>2+</sup> acted on Cr(VI) reduction by the sequence of Mg<sup>2+</sup> > Zn<sup>2+</sup>, and the corresponding removal rates were inhibited by 60.15% and 33.55%. The second-order  $k$  also accordingly decreased, which were 0.009 M<sup>-1</sup> min<sup>-1</sup> (Mg<sup>2+</sup>) and 0.026 M<sup>-1</sup> min<sup>-1</sup> (Zn<sup>2+</sup>), respectively. Since that the redox potential of Zn<sup>2+</sup> and Mg<sup>2+</sup> were -0.76 V and -2.36 V, which was higher than that of Cr<sub>2</sub>O<sub>7</sub><sup>2-</sup> (+1.33 V), the reduction of Zn<sup>2+</sup> and Mg<sup>2+</sup> could not occurred on the photocathode [22]. Therefore, the negative influence of Zn<sup>2+</sup> and Mg<sup>2+</sup> on Cr(VI) removal was mainly for their occupation on part of the adsorption sites of Cr(VI).

Inspired by the effective participation of photogenerated carriers in the dual-FH-TiO<sub>2</sub>/Ti PEC system, we proposed an innovative strategy to simultaneously reach the effective pollutant removal under the premise of the coexistence of BPA and Cr(VI), making full use of photoinduced  $e^-/h^+$ . Fig. S11a illustrated that the removal of BPA (97.82%, 30 min) was much heightened with the coexistence of Cr(VI), in distinct contrast to that of 79.08% when BPA was considered as the single pollutant. The first-order  $k$  in the presence of Cr(VI) was about 0.128 min<sup>-1</sup>, 2.4 folds with separate BPA removal (Fig. S11b). Furthermore, the 99.17% of Cr(VI) was reduced with the joint devotion of BPA in only 30 min, 1.13 times that of only Cr(VI) was added. The second order  $k$  promoted to 1.91 M<sup>-1</sup> min<sup>-1</sup>, in marked comparison with that of 0.137 M<sup>-1</sup> min<sup>-1</sup> with the system of Cr(VI) alone. This result unambiguously suggested a mutually reinforcing relationship in the dual-FH-TiO<sub>2</sub>/Ti PEC system between BPA and Cr(VI). The increased separation and utilization of photogenerated carriers provided a prerequisite for the removal of BPA and Cr(VI). Additionally, Cr(VI) participated in the bridge cleavage and ring-opening reactions of BPA, further boosting the mineralization of BPA [13].

Furthermore, the stability of photoelectrode was also considered. The oxidation efficiency of BPA (Fig. S12a) and the reduction efficiency of Cr(VI) (Fig. S12b) in the dual-FH-TiO<sub>2</sub>/Ti PEC system successfully remained at 95.22% and 98.15% after 5 runs, displaying the gratifying removal efficiency. And the regeneration of catalyst surface was realized via a certain time reaction at 0.4 V in 0.1 M Na<sub>2</sub>SO<sub>4</sub> under irradiation when the used 3D FH-TiO<sub>2</sub>/Ti was taken as the anode, while Pt as the cathode. The SEM images of 3D FH-TiO<sub>2</sub>/Ti after 5 cycles were presented in Fig. S13, and the 3D structure of photoelectrode was well maintained. The slight declination in removal was owing to the chemical bonding of Cr(III) [1] on the 3D FH-TiO<sub>2</sub>/Ti photoelectrodes that was observed by XPS technology (Fig. S14). Therefore, the desorption of Cr(III) was a key step for recycling of the 3D FH-TiO<sub>2</sub>/Ti photoelectrodes, and was regarded as the focus of future work.

## 4. Conclusion

Industrial wastewater is one of the main pollution sources worldwide, where heavy metals and EDCs are concurrently detected, such as BPA and Cr(VI), even after conventional treatment, bringing about high toxicity, and a complex water matrix. Further treatment targeting to the highly efficient removal of BPA and Cr(VI), especially achieving synchronous oxidation and reduction in the redox system.

In conclusion, a novel tactic was provided for the simultaneous removal of BPA and Cr(VI) via constructing the synchronous redox PEC system over dual 3D FH-TiO<sub>2</sub>/Ti photoelectrodes. Almost 100% removal of BPA and Cr(VI) was realized in the stimulated wastewater only in 30 min, and the corresponding efficiency reach 97.04% and 81.18% in the practical wastewater, respectively. The high removal capacity has been confirmed to be attributed to the effective charge separation of 3D FH-TiO<sub>2</sub>/Ti, the synergistic effect of photocathode and photoanode. This study paves the way for designing and discovering innovative synchronous redox PEC system for the simultaneous removal of heavy metals and EDCs.

## CRediT authorship contribution statement

**Yiqiong Hu:** Conceptualization, Investigation, Methodology, Data curation, Writing – original draft. **Yuzhou Jin:** Methodology, Data curation. **Pan Zhang:** Writing – review & editing. **Ya-nan Zhang:** Supervision, Funding acquisition, Writing – review & editing. **Guohua Zhao:** Supervision, Project administration, Formal analysis.

## Declaration of Competing Interest

The authors declare that they have no known competing financial interests or personal relationships that could have appeared to influence the work reported in this paper.

## Data availability

Data will be made available on request.

## Acknowledgment

This work was supported by the National Natural Science Foundation of China (NSFC, No. 22276136, 21876133, 22076140, 21876128), Natural Science Foundation of Shanghai (No. 20ZR1462500), the Science & Technology Commission of Shanghai Municipality (No. 14DZ2261100) and the Fundamental Research Funds for the Central Universities (No. 22120210531, 2022-4-YB-1B).

## Appendix A. Supporting information

Supplementary data associated with this article can be found in the online version at [doi:10.1016/j.apcatb.2022.122102](https://doi.org/10.1016/j.apcatb.2022.122102).

## References

- Q. Ge, X. Feng, R. Wang, R. Zheng, S. Luo, L. Duan, Y. Ji, J. Lin, H. Chen, Mixed redox-couple-involved chalcopyrite phase CuFeS<sub>2</sub> quantum dots for highly efficient Cr(VI) removal, *Environ. Sci. Technol.* 54 (2020) 8022–8031.
- J. Li, C. Xiao, K. Wang, Y. Li, G. Zhang, Enhanced generation of reactive oxygen species under visible light irradiation by adjusting the exposed facet of FeWO<sub>4</sub> nanosheets to activate oxalic acid for organic pollutant removal and Cr(VI) reduction, *Environ. Sci. Technol.* 53 (2019) 11023–11030, <https://doi.org/10.1021/acs.est.9b00641>.
- J. Qu, Y. Wang, X. Tian, Z. Jiang, F. Deng, Y. Tao, Q. Jiang, L. Wang, Y. Zhang, KOH-activated porous biochar with high specific surface area for adsorptive removal of chromium (VI) and naphthalene from water: affecting factors, mechanisms and reusability exploration, *J. Hazard. Mater.* 401 (2021), 123292.
- B. Zhang, Y. He, H. Zhu, X. Huang, X. Bai, K. Kannan, T. Zhang, Concentrations of bisphenol A and its alternatives in paired maternal-fetal urine, serum and amniotic fluid from an e-waste dismantling area in China, *Environ. Int.* 136 (2020), 105407.
- C. Xiao, L. Wang, Q. Zhou, X. Huang, Hazards of bisphenol A (BPA) exposure: a systematic review of plant toxicology studies, *J. Hazard. Mater.* 384 (2020), 121488.
- Y. Ma, H. Liu, J. Wu, L. Yuan, Y. Wang, X. Du, R. Wang, P.W. Marwa, P. Petlulu, X. Chen, H. Zhang, The adverse health effects of bisphenol A and related toxicity mechanisms, *Environ. Res.* 176 (2019), 108575.
- Y.Q. Huang, C.K. Wong, J.S. Zheng, H. Bouwman, R. Barra, B. Wahlstrom, L. Neretin, M.H. Wong, Bisphenol A (BPA) in China: a review of sources, environmental levels, and potential human health impacts, *Environ. Int.* 42 (2012) 91–99.
- E. Yamazaki, N. Yamashita, S. Taniyasu, J. Lam, P.K.S. Lam, H.B. Moon, Y. Jeong, P. Kannan, H. Achyuthan, N. Munuswamy, K. Kannan, Bisphenol A and other bisphenol analogues including BPS and BPF in surface water samples from Japan, China, Korea and India, *Ecotoxicol. Environ. Saf.* 122 (2015) 565–572.
- Y. Zhang, M. Xu, H. Li, H. Ge, Z. Bian, The enhanced photoreduction of Cr(VI) to Cr(III) using carbon dots coupled TiO<sub>2</sub> mesocrystals, *Appl. Catal. B Environ.* 226 (2018) 213–219.
- Y. Huang, B. Zhou, R. Han, X. Lu, S. Li, N. Li, Spatial-temporal characteristics and driving factors of the human health impacts of five industrial aquatic toxic metals in China, *Environ. Monit. Assess.* 192 (2020) 290.
- Q. Liang, S. Ploychompoo, J. Chen, T. Zhou, H. Luo, Simultaneous Cr(VI) reduction and bisphenol A degradation by a 3D Z-scheme Bi<sub>2</sub>S<sub>3</sub>-BiVO<sub>4</sub> graphene aerogel under visible light, 2020, *Chem. Eng. J.* 384 (2020), 123256.
- K. Xiao, J. He, J. Zhang, B. Yang, X. Zhao, Simultaneous Cr(VI) removal and bisphenol A degradation in a solar-driven photocatalytic fuel cell with dopamine modified carbon felt cathode, *Appl. Surf. Sci.* 471 (2019) 912–920.
- Y. Zhang, D. Zhang, L. Zhou, Y. Zhao, J. Chen, Z. Chen, F. Wang, Polypyrrole/reduced graphene oxide aerogel particle electrodes for high-efficiency electrocatalytic synergistic removal of Cr(VI) and bisphenol A, *Chem. Eng. J.* 336 (2018) 690–700.
- P.Y. Nguyen, G. Carvalho, M.A.M. Reis, A. Oehmen, A review of the biotransformations of priority pharmaceuticals in biological wastewater treatment processes, *Water Res.* 188 (2021), 116446.
- W.S. Chai, J.Y. Cheun, P.S. Kumar, M. Mubashir, Z. Majeed, F. Banat, S.H. Ho, P. L. Show, A review on conventional and novel materials towards heavy metal adsorption in wastewater treatment application, 2021, *J. Clean. Prod.* 296 (2021), 126589.
- X. Zhao, X. Wang, T. Lou, Preparation of fibrous chitosan/sodium alginate composite foams for the adsorption of cationic and anionic dyes, *J. Hazard. Mater.* 403 (2021), 124054.
- G. Zhao, Y. Sun, Y. Zhao, T. Wen, X. Wang, Z. Chen, G. Sheng, C. Chen, X. Wang, Enhanced photocatalytic simultaneous removals of Cr(VI) and Bisphenol A over Co(II)-modified TiO<sub>2</sub>, *Langmuir* 35 (2019) 276–283.
- Y.X. Li, X. Wang, C.C. Wang, H. Fu, Y. Liu, P. Wang, C. Zhao, S-TiO<sub>2</sub>/UiO-66-NH<sub>2</sub> composite for boosted photocatalytic Cr(VI) reduction and bisphenol A degradation under LED visible light, *J. Hazard. Mater.* 399 (2020), 123085.
- H. Wang, Q. Li, S. Zhang, Z. Chen, W. Wang, G. Zhao, L. Zhuang, B. Hu, X. Wang, Visible-light-driven N<sub>2</sub>-g-C<sub>3</sub>N<sub>4</sub> as a highly stable and efficient photocatalyst for bisphenol A and Cr(VI) removal in binary systems, *Catal. Today* 335 (2019) 110–116.
- Z. Wu, X. Yuan, G. Zeng, L. Jiang, H. Zhong, Y. Xie, H. Wang, X. Chen, H. Wang, Highly efficient photocatalytic activity and mechanism of Yb<sup>3+</sup>/Tm<sup>3+</sup> codoped In<sub>2</sub>S<sub>3</sub> from ultraviolet to near infrared light towards chromium (VI) reduction and rhodamine B oxidative degradation, *Appl. Catal. B Environ.* 225 (2018) 8–21.
- W. Yang, R.R. Prabhakar, J. Tan, S.D. Tilley, J. Moon, Strategies for enhancing the photocurrent, photovoltage, and stability of photoelectrodes for photoelectrochemical water splitting, *Chem. Soc. Rev.* 48 (2019) 4979–5015.
- W. Cui, J. He, H. Wang, J. Hu, L. Liu, Y. Liang, Polyaniline hybridization promotes photo-electro-catalytic removal of organic contaminants over 3D network structure of rGH-PANI/TiO<sub>2</sub> hydrogel, *Appl. Catal. B Environ.* 232 (2018) 232–245.
- H. Rajput, E.E. Kwon, S.A. Younis, S. Weon, T.H. Jeon, W. Choi, K.H. Kim, Photoelectrocatalysis as a high-efficiency platform for pulping wastewater treatment and energy production, *Chem. Eng. J.* 412 (2021), 128612.
- M.C. Collivignarelli, A. Abba, M. Carnevale Miino, G. Bertanza, S. Sorlini, S. Damiani, H. Arab, M. Bestetti, S. Franz, Photoelectrocatalysis on TiO<sub>2</sub> meshes: different applications in the integrated urban water management, *Environ. Sci. Pollut. Res. Int.* 28 (2021) 59452–59461.
- X. Liu, H. Zhang, C. Liu, J. Chen, G. Li, T. An, P.K. Wong, H. Zhao, UV and visible light photoelectrocatalytic bactericidal performance of 100% {111} faceted rutile TiO<sub>2</sub> photoanode, *Catal. Today* 224 (2014) 77–82.
- H. Zhang, X. Liu, Y. Wang, P. Liu, W. Cai, G. Zhu, H. Yang, H. Zhao, Rutile TiO<sub>2</sub> films with 100% exposed pyramid-shaped {111} surface: photoelectron transport properties under UV and visible light irradiation, *J. Mater. Chem. A* 1 (2013) 2642–2652.
- M. Sayed, L.A. Shah, J.A. Khan, N.S. Shah, J. Nisar, H.M. Khan, P. Zhang, A. R. Khan, Efficient photocatalytic degradation of norfloxacin in aqueous media by hydrothermally synthesized immobilized TiO<sub>2</sub>/Ti films with exposed {001} facets, *J. Phys. Chem. A* 120 (2016) 9916–9931.
- S. Selcuk, A. Selloni, Facet-dependent trapping and dynamics of excess electrons at anatase TiO<sub>2</sub> surfaces and aqueous interfaces, *Nat. Mater.* 15 (2016) 1107–1112.
- N. Roy, Y. Sohn, D. Pradhan, Synergy of low-energy {101} and high-energy {001} TiO<sub>2</sub> crystal facets for enhanced photocatalysis, *ACS Nano* 7 (2013) 2532–2540.
- X. Gu, N. Qin, P. Zhang, Y. Hu, Y. Zhang, G. Zhao, In-situ synthesis of {111}TiO<sub>2</sub>/Ti photoelectrode to boost efficient removal of dimethyl phthalate based on a bi-functional interface, *Chem. Eng. J.* 422 (2021), 129980.



- [31] R. Song, H. Chi, Q. Ma, D. Li, X. Wang, W. Gao, H. Wang, X. Wang, Z. Li, C. Li, Highly efficient degradation of persistent pollutants with 3D nanocone TiO<sub>2</sub>-based photoelectrocatalysis, *J. Am. Chem. Soc.* 143 (2021) 13664–13674.
- [32] C. Gao, T. Wei, Y. Zhang, X. Song, Y. Huan, H. Liu, M. Zhao, J. Yu, X. Chen, A photoresponsive rutile TiO<sub>2</sub> Heterojunction with enhanced electron-hole separation for high-performance hydrogen evolution, *Adv. Mater.* 31 (2019), e1806596.
- [33] S. Lee, I. Cho, J. Noh, K. Hong, G. Han, H. Jung, S. Jeong, C. Lee, H. Shin, Correlation of anatase particle size with photocatalytic properties, *Phys. Status Solidi* 207 (2010) 2288–2291.
- [34] L. Sun, Y. Qin, Q. Cao, B. Hu, Z. Huang, L. Ye, X. Tang, Novel photocatalytic antibacterial activity of TiO<sub>2</sub> microspheres exposing 100% reactive {111} facets, *Chem. Commun.* 47 (2011) 12628–12630.
- [35] X. Noifalisse, F. Renaux, D. Cossement, N. Sebaihi, R. Lazzaroni, R. Snyder, Effect of the crystalline constitution of TiO<sub>2</sub> substrates on the growth of ultrathin Mo layer, *Surf. Sci.* 606 (2012) 1680–1684.
- [36] H. Ji, P. Du, D. Zhao, S. Li, F. Sun, E.C. Duin, W. Liu, 2D/1D graphitic carbon nitride/titanate nanotubes heterostructure for efficient photocatalysis of sulfamethazine under solar light: catalytic “hot spots” at the rutile–anatase–titanate interfaces, *Appl. Catal. B Environ.* 263 (2020), 118357.
- [37] T. Wei, W. Lau, X. An, X. Yu, Interfacial charge transfer in MoS<sub>2</sub>/TiO<sub>2</sub> heterostructured photocatalysts: the impact of crystal facets and defects, *Molecules* 24 (2019) 1769.
- [38] C. Li, T. Wang, Z. Zhao, W. Yang, J. Li, A. Li, Z. Yang, G.A. Ozin, J. Gong, Promoted fixation of molecular nitrogen with surface oxygen vacancies on plasmon-enhanced TiO<sub>2</sub> photoelectrodes, *Angew. Chem. Int. Ed.* 57 (2018) 5278–5282.
- [39] X. Deng, H. Zhang, R. Guo, Q. Ma, Y. Cui, X. Cheng, M. Xie, Q. Cheng, Effect of Ti<sup>3+</sup> on enhancing photocatalytic and photoelectrochemical properties of TiO<sub>2</sub> nanorods/nanosheets photoelectrode, *Sep. Purif. Technol.* 192 (2018) 329–339.
- [40] M.Y. Lee, I. Ahmed, K. Yu, C.S. Lee, K.K. Kang, M.S. Jang, W.S. Ahn, Aqueous adsorption of bisphenol A over a porphyrinic porous organic polymer, *Chemosphere* 265 (2021), 129161.
- [41] G. Zhou, Y. Cao, Y. Jin, C. Wang, Y. Wang, C. Hua, S. Wu, Novel selective adsorption and photodegradation of BPA by molecularly imprinted sulfur doped nano-titanium dioxide, *J. Clean. Prod.* 274 (2020), 122929.
- [42] S. Mamman, F.B.M. Suah, M. Raao, F.S. Mehamod, S. Asman, N.N.M. Zain, Removal of bisphenol A from aqueous media using a highly selective adsorbent of hybridization cyclodextrin with magnetic molecularly imprinted polymer, *R. Soc. Open Sci.* 8 (2021), 201604.
- [43] National Institute of Materials and Chemical Research, Spectral Database for Organic Compounds (SDBS). ([https://sdb.sdb.aist.go.jp/sdb/cgi-bin/direct\\_frame\\_top.cgi](https://sdb.sdb.aist.go.jp/sdb/cgi-bin/direct_frame_top.cgi)), 2022, (accessed 20 May 2022).
- [44] X. Li, C. Guo, X. Jin, C. He, Q. Yao, G. Lu, Z. Dang, Mechanisms of Cr(VI) adsorption on schwertmannite under environmental disturbance: changes in surface complex structures, *J. Hazard. Mater.* 416 (2021), 125781.
- [45] A. Dali, I.E. Boulguemh, F. Louafi, C. Mouats, Synthesis, characterization and environmental application of an original adsorbent: polyaniline-coated luffa cylindrica, *J. Polym. Res.* 28 (2021) 33.
- [46] B. Liu, X. Zhao, The synergetic effect of V and Fe-co-doping in TiO<sub>2</sub> studied from the DFT + U first-principle calculation, *Appl. Surf. Sci.* 399 (2017) 654–662.
- [47] A. Yu, Shi Zhan, L. Qiu, X. Wang, H. Yang, Y. Li, Ultraviolet detector with ultrahigh responsivity based on Anatase TiO<sub>2</sub> nanotubes array modified with (001) exposed nanofacets, *Vacuum* 151 (2018) 237–242.
- [48] Y. Yu, X. Yang, Y. Zhao, X. Zhang, L. An, M. Huang, G. Chen, R. Zhang, Engineering the band gap states of the rutile TiO<sub>2</sub>(110) surface by modulating the active heteroatom, *Angew. Chem. Int. Ed.* 57 (2018) 8550–8554.
- [49] Y. Hu, X. Gu, G. Zhao, Y.N. Zhang, In situ construction of 3D TiO<sub>2</sub> photoelectrode with multilevel facet heterojunctions towards the efficient removal of bisphenol A, *Chem. Commun.* 57 (2021) 7633–7636.
- [50] H. Tang, Q. Shang, Y. Tang, X. Yi, Y. Wei, K. Yin, M. Liu, C. Liu, Static and continuous flow photoelectrocatalytic treatment of antibiotic wastewater over mesh of TiO<sub>2</sub> nanotubes implanted with g-C<sub>3</sub>N<sub>4</sub> nanosheets, *J. Hazard. Mater.* 384 (2020), 121248.
- [51] T.S. Bui, P. Bansal, B.K. Lee, T. Mahvelati-Shamsabadi, T. Soltani, Facile fabrication of novel Ba-doped g-C<sub>3</sub>N<sub>4</sub> photocatalyst with remarkably enhanced photocatalytic activity towards tetracycline elimination under visible-light irradiation, *Appl. Surf. Sci.* 506 (2020), 144184.
- [52] Z. Yuan, H. Huang, N. Li, D. Chen, Q. Xu, H. Li, J. He, J. Lu, All-solid-state WO<sub>3</sub>/TQDs/In<sub>2</sub>S<sub>3</sub> Z-scheme heterojunctions bridged by Ti<sub>3</sub>C<sub>2</sub> quantum dots for efficient removal of hexavalent chromium and bisphenol A, *J. Hazard. Mater.* 409 (2021), 125027.
- [53] G. Dong, L. Zhang, Synthesis and enhanced Cr(VI) photoreduction property of formate anion containing graphitic carbon nitride, *J. Phys. Chem. C* 117 (2013) 4062–4068.
- [54] H.T. Nguyen, J. Lee, E. Kwon, G. Lisak, B.X. Thanh, F. Ghanbari, K.A. Lin, Bamboo-like N-doped carbon nanotube-confined cobalt as an efficient and robust catalyst for activating monopersulfate to degrade bisphenol A, *Chemosphere* 279 (2021), 130569.
- [55] H. Wang, W. Guo, Q. Si, B. Liu, Q. Zhao, H. Luo, N. Ren, Multipath elimination of bisphenol A over bifunctional polymeric carbon nitride/biochar hybrids in the presence of persulfate and visible light, *J. Hazard. Mater.* 417 (2021), 126008.
- [56] C. Li, Y. Guo, D. Tang, Y. Guo, G. Wang, H. Jiang, J. Li, Optimizing electron structure of Zn-doped AgFeO<sub>2</sub> with abundant oxygen vacancies to boost photocatalytic activity for Cr(VI) reduction and organic pollutants decomposition: DFT insights and experimental, *Chem. Eng. J.* 411 (2021), 128515.
- [57] Y. Lv, H. Liu, D. Jin, H. Yang, D. He, Z. Zhang, Y. Zhang, J. Qu, Y.-N. Zhang, Effective degradation of norfloxacin on Ag<sub>3</sub>PO<sub>4</sub>/CNTs photoanode: Z-scheme mechanism, reaction pathway, and toxicity assessment, *Chem. Eng. J.* 429 (2022), 132092.
- [58] E.D. Du, X.X. Feng, Y.Q. Guo, M.G. Peng, H.Q. Feng, J.L. Wang, S. Zhang, Dimethyl phthalate degradation by UV/H<sub>2</sub>O<sub>2</sub>: combination of experimental methods and quantum chemical calculation, *CLEAN Soil Air Water* 43 (2015) 811–821.
- [59] J. Mack, J.R. Bolton, Photochemistry of nitrite and nitrate in aqueous solution: a review, *J. Photochem. Photobiol. A* 128 (1999) 1–13.